



## ISTITUTO NAZIONALE DI RICERCA METROLOGICA Repository Istituzionale

Epoxy nanocomposites functionalized with in situ generated magnetite nanocrystals:  
Microstructure, magnetic properties, interaction among magnetic particles

This is the author's submitted version of the contribution published as:

*Original*

Epoxy nanocomposites functionalized with in situ generated magnetite nanocrystals: Microstructure, magnetic properties, interaction among magnetic particles / Sciancalepore, C; Bondioli, F; Messori, M; Barrera, G; Tiberto, PAOLA MARIA; Allia, P.. - In: POLYMER. - ISSN 0032-3861. - 59:(2015), pp. 278-289. [10.1016/j.polymer.2014.12.047]

*Availability:*

This version is available at: 11696/29938 since:

*Publisher:*

Elsevier

*Published*

DOI:10.1016/j.polymer.2014.12.047

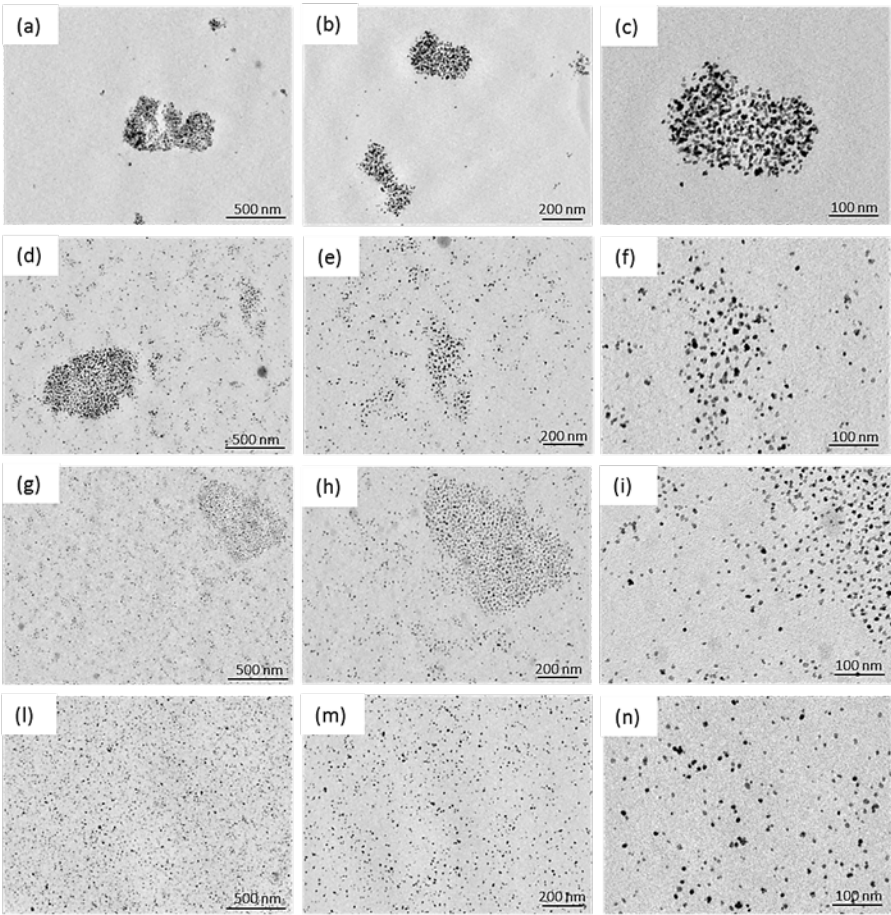
*Terms of use:*

This article is made available under terms and conditions as specified in the corresponding bibliographic description in the repository

*Publisher copyright*

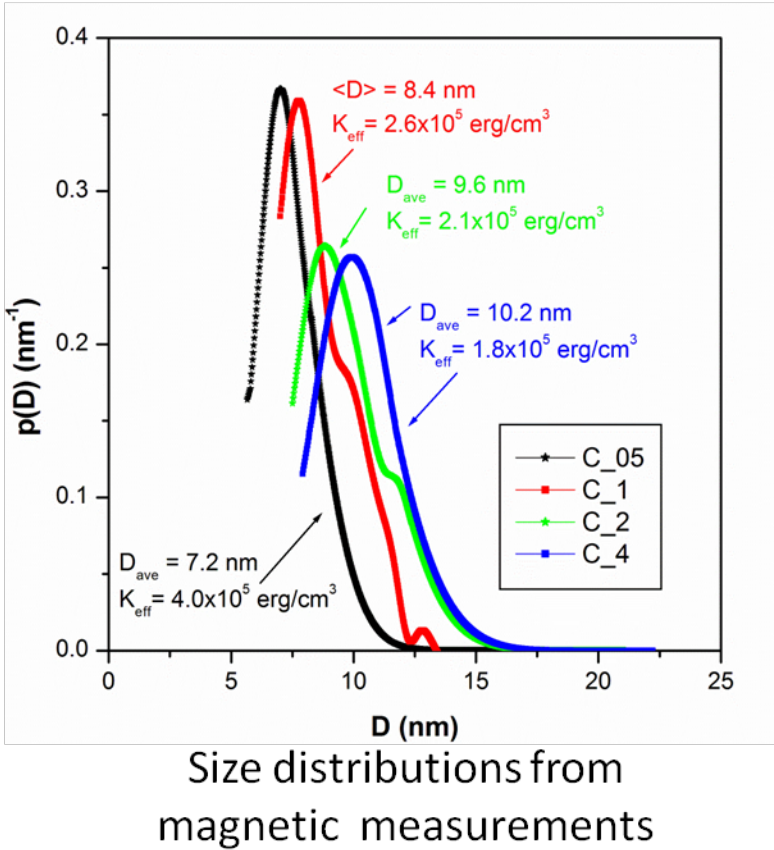
(Article begins on next page)

TEM images of magnetic nanocomposites



increasing concentration

increasing magnification



# Epoxy nanocomposites obtained through an innovative route and functionalized with *in situ* generated magnetite nanocrystals: microstructure, magnetic properties, interaction among magnetic particles.

C. Sciancalepore,<sup>a</sup> F. Bondioli,<sup>b</sup> M. Messori,<sup>a</sup> G. Barrera,<sup>c</sup> P. Tiberto<sup>d</sup> and P. Allia<sup>e,\*</sup>,

<sup>a</sup> Department of Engineering “Enzo Ferrari”, Via Vignolese 905, 41125 Modena (Italy).

<sup>b</sup> Department of Industrial Engineering, Parco Area delle Scienze 181/A, 43124 Parma (Italy).

<sup>c</sup> University of Torino, Department of Chemistry, Via Pietro Giuria 7, 10125 Torino (Italy).

<sup>d</sup> I.N.Ri.M., Electromagnetism, Strada delle Cacce 91, 10138 Torino (Italy).

<sup>e</sup> Politecnico di Torino, DISAT, Corso Duca degli Abruzzi 24, 10129 Torino (Italy).

## Abstract

Magnetite nanoparticles in the range 7-10.5 nm were prepared by non hydrolytic sol-gel (NHSG) process in the presence of benzyl alcohol in different concentrations. The suspensions were mixed with bisphenol A diglycidyl ether (DGEBA) and cured in the presence of ytterbium(III) trifluoromethanesulfonate as cationic initiator. Magnetite nanoparticles and epoxy nanocomposites were characterized by structural, chemical and magnetic techniques. A procedure of data analysis is proposed to determine value, sign and surface contribution of the magnetic anisotropy of nanoparticles by comparing the information gained from field-cooled/zero-field-cooled magnetization curves and TEM images. Above blocking temperature, the nanoparticles dispersed in the epoxy resin give rise to an interacting superparamagnetic system and follow the corresponding scaling law. A model explains why the magnetic interaction energy depends not only on nanoparticle concentration in the epoxy but also on concentration fluctuations, being larger in samples where the nanoparticle dispersion is not uniform..

## 1. Introduction

In recent years, considerable efforts have been devoted to the design and controlled fabrication of nanostructured materials showing specific physico-chemical properties [1]. In particular, nanocomposites, which combine inorganic nanoparticles and organic polymeric matrices, allow one to get new advanced

---

\* Corresponding author. Tel.: +39 110907336  
E-mail addresses: [paolo.allia@polito.it](mailto:paolo.allia@polito.it) (Paolo Allia)

materials showing not only a dramatic improvement in mechanical properties [2] but also innovative functional properties[3]. Among other properties, the magnetic behaviour of polymeric nanocomposites has been recently investigated for potential application in electronic, magnetic and photonic devices, gas and vapour sensors, non linear optic systems, photovoltaic solar cells and biomedical applications [4-6]. Most of the existing literature is related to the synthesis of nanosized powders where the polymer phase is used to modify the surface chemistry of magnetic nanoparticles in order to prevent their aggregation into large clusters; however, recent studies have been aimed to obtain magnetic nanocomposite materials. The main approach involves the use of preformed magnetite nanoparticles, generally obtained by chemical precipitation starting from ferric chloride [7]. In order to prevent the nanoparticle agglomeration and to ensure compatibility between the nanoparticles and the polymer matrix, oleic acid is generally used as a surfactant, e.g., to successfully incorporate magnetite in poly(methyl methacrylate) (PMMA) [8,9], or hydrogenated epoxy resin (HDGBA) [10]. Recently, Guo *et al.* [11] used a conductive polypyrrole coating on nanomagnetite as a coupling agent to obtain reinforced magnetic epoxy nanocomposites.

An alternative strategy is represented by *in situ* synthesis that uses chemical reactions in a liquid environment to generate nanocomposites [12]. The common feature is that nanoparticles are synthesized in a first step, mostly as a sol or dispersed in a solution, followed by a second step where a monomer or resin is added and brought to polymerization. Among the different synthetic procedures, the sol-gel chemistry represents one of the preferred preparation routes, thanks to its mild conditions that become strategic when organic materials are involved in the process permitting to avoid their thermal degradation. Typical precursors are metal alkoxides which reacting with water give rise to nanoparticles having narrow grain size distribution with dimensions ranging from 5 to 100 nm [13]. Alternatively to the aqueous route, the so-called non-hydrolytic sol-gel (NHSG) reaction can also be used to obtain very pure and crystalline metal oxides [14-17]. As well as the aqueous route, the NHSG process is divided in two steps. The first step involves the reaction of a metal halide, alkoxide or acetylacetonate with an organic oxygen donor (such as alcohols, ether, etc.). The second step (condensation) can follow different pathways depending on the selected precursor. The presence in the reactive system of an organic oligomer or polymer (either bearing or not suitable groups reactive towards to the sol-gel process) leads to the formation of organic-inorganic hybrid structures composed of metal oxide and organic phases intimately mixed with each other. In principle, the NHSG route gives access to a wide range of organic-inorganic nanocomposite products similar to those accessible using the hydrolytic route [18-20]. In practice, however, differences arising from the nature of the precursors, the choice of possible solvents and the different mechanisms of the reactions may dictate the type of hybrid material which can be prepared by either route. In general terms, with respect to the hydrolytic counterpart, it is recognized [21] that the NHSG process is potentially solvent-free, without problems with hydrophobic substances, and particularly suitable for water-sensitive species. On the other hand, the formation of by-products and their potential incompatibility with O-containing species have to be taken into account as possible negative aspects.

Magnetite nanoparticles are a case study for checking current views and models describing magnetic nanomaterials. In fact, most chemical routes to synthesize ferrimagnetic Fe-oxide nanoparticles [22] have a reproducible output, a well-defined chemical composition and structure, a narrow spread of sizes/shapes. Magnetic nanocomposites containing Fe-oxide nanoparticles are attracting widespread attention from a fundamentalist's viewpoint and because of their prospective application also. Applications are mostly related to the physical properties resulting from the combination of a magnetic dispersoid and a host matrix [23] and include functionally graded materials [24] and/or sensing elements in the area of information and communication technologies (ICTs) [25].

Various magnetic properties of magnetite nanoparticles (NPs) including spontaneous magnetization, coercive field, magnetic interactions are affected by their surroundings [22]. The experimental evidence points to a substantial role played by the magnetic interactions among particles, which can be remarkably modified by nanoparticle concentration and/or by the hosting material. In systems where contact interactions are minimized, magnetic dipolar interaction plays a central role. Systematic measurements indicate that the influence of dipolar interaction is not confined to the low-temperature domain [26], significant effects being measured even at room temperature. In fact, departures from the superparamagnetic scaling law are typically observed in many nanoparticle systems; these can be satisfactorily accounted for by a model of interacting superparamagnetism (the ISP model) [27], basically a mean-field theory applied to temperatures where the dipolar interaction energy is comparable in magnitude to the thermal energy  $k_B T$ . The region where this condition is applicable extends over hundreds of Kelvin in typical nanoparticle systems, up to room temperature in several cases. This makes the ISP model interesting not only from a fundamentalist's standpoint but also in view of applications.

Aim of the present work was the preparation of innovative nanocomposites through the *in situ* generation of magnetite nanoparticles within a suspending medium, which can also undergo a subsequent polymerization in the presence of aliphatic epoxy resin (bisphenol A diglycidyl ether, DGEBA). To do this, the so-called 'benzyl alcohol route' [15] was used to prepare magnetite nanoparticles suspended in benzyl alcohol which was also reactive towards the polymerization of epoxy resins induced by cationic initiators. In a recent work, we reported the use of this innovative procedure to obtain magnetic composites using a UV-curable cycloaliphatic epoxy resin [28]. The cationic photo-polymerization produced a three-dimensional network in which the suspending medium (benzyl alcohol) was covalently linked to the epoxy network according to the 'activated monomer' mechanism during the propagation step in the cationic ring-opening polymerization. In all nanocomposites obtained in this way the magnetic behaviour could be safely ascribed to individual, independent magnetic entities having sizes corresponding to a single magnetite nanoparticle demonstrating that the chosen strategy allowed us to obtain homogeneous composite materials, the inorganic particles being homogeneously distributed and well dispersed within the polymeric matrix.

In the present work, the same approach was used in order to verify the possibility to incorporate magnetite suspensions in benzyl alcohol with epoxy resin by means of a thermally activated cationic polymerization instead of the UV-curing process. The prepared magnetite nanoparticles and epoxy composites were fully characterized with the specific aim to correlate the composite microstructures with their magnetic properties.

In particular, a study of equilibrium magnetic properties was conducted on four dried nanopowders differing by a single preparation parameter (the  $\text{Fe}(\text{AcAc})_3\text{:BzOH}$  ratio) and four nanocomposites containing the as-prepared nanoparticles in different amounts. The results of the measurements of the static magnetic properties are combined with well-assessed structural/morphological data. In this way, it is possible to determine a reliable value of the effective magnetic anisotropy of the nanoparticles singling out the contribution from the surface (in both magnitude and sign), and to measure the effects of dipolar interaction in the nanocomposites. The magnetic interactions are tuned not only by nanoparticle concentration in the epoxy resin but also by a more or less uniform distribution of the nanoparticles. The magnetic properties are well described by the ISP model over the entire range of investigated temperatures.

## **2. Experimental**

### **2.1 Materials**

Bisphenol A diglycidyl ether (DGEBA, Dow D.E.R.<sup>TM</sup> 332 with an epoxide equivalent weight of 172-176), benzyl alcohol (BzOH), ytterbium(III) trifluoromethanesulfonate hydrate ( $\text{Yb}(\text{OTf})_3$ ), and ethanol (EtOH) were purchased by Sigma Aldrich (Milan, Italy).

Acetylacetone (AcAcH) and iron(III)chloride exahydrate ( $\text{FeCl}_3 \cdot 6\text{H}_2\text{O}$ ) were purchased from Carlo Erba (Milan, Italy).

All materials were high purity reactants and were used as received without any further purification.

### **2.2 Synthesis of magnetite alcoholic suspensions**

In a 100 mL Schlenk tube 1.00 g (2.83 mmol) of Iron(III)-acetylacetonate ( $\text{Fe}(\text{AcAc})_3$ ), synthesized as reported in Bondioli et al.,<sup>13</sup> was dissolved in different amount of BzOH in order to evaluate the effect of the  $\text{Fe}(\text{AcAc})_3\text{:BzOH}$  ratio on the powder properties (see composition details in Table 1). The reaction was left stirring at room temperature for 15 min and then heated to 200 °C in an oil bath for 48 hrs. After reaction a stable suspension was obtained. To better characterize the inorganic phase, the obtained powders were dispersed in methanol with an ultrasonic bath and centrifuged at 4000 rpm for 60 min; the powders were washed, centrifuged till the obtainment of a colorless liquid phase and finally dried under reduced pressure.

**Table 1:**

Composition of the NHSG reaction batches and morphology of the obtained powders

Fe <sub>2</sub> O <sub>3</sub> powder Code	Fe(AcAc) <sub>3</sub> (g)	BzOH (g)	Fe(AcAc) <sub>3</sub> :BzOH Ratio	TEM size (nm)	Aspect ratio
Fe1	1.00	31.1	0.03	7.2±0.9	1.13±0.09
Fe2		15.6	0.06	8.4±1	1.12±0.07
Fe3		7.77	0.12	9.6±1.6	1.20±0.10
Fe4		3.87	0.24	10.2±1.7	1.18±0.15

### 2.3 Characterization of magnetite powders

Crystalline phase of the synthesized powders were analyzed by X-ray powder diffraction technique using an X'Pert PRO diffractometer (PANalytical, Netherlands), powered by a Philips PW3373/10 Cu LFF DK388689 X-ray generator and fitted with an X'Celerator detector. Diffraction data were acquired by exposing powder samples to Cu-K $\alpha$  X-ray radiation with a characteristic wavelength ( $\lambda$ ) of 1.5418 Å. X-rays were generated from a Cu anode supplied with 40 kV and a current of 40 mA. The X-ray diffraction (XRD) patterns were collected at room temperature in 10-70° 2 $\theta$  range, with a step size of 0.0167° and a nominal time per step of 0.008°·s<sup>-1</sup>. Fixed anti-scatter and divergence slits of 1/2° were used together with a beam mask of 10 mm and all scans were carried out in 'continuous' scanning mode. The average crystallite size was calculated using the Scherrer method [29], based on the calculus of the integral breadth of the X-ray diffraction peaks.

Raman-scattering experiments were carried out using a micro-Raman system (Labram instrument Jobin Yvon-Horiba, Japan) at room temperature. The 632.81 nm line of He-Ne laser with an exposure time of 60 s was used for excitation.

Particles morphology was examined by transmission electron microscopy (TEM, JEM 2010, Jeol, Japan). A drop of the obtained suspensions was placed on a copper grid (200 mesh) covered with PELCO® support films of Formvar (thickness of 30-60 nm), followed by drying. Particles size distribution analysis was performed on the obtained images with the SPIP (Scanning Probe Imaging Processor, Image Metrology A/S, Denmark) software. A minimum of 100 particles was measured for each powder in order to obtain a good statistical approximation.

In order to investigate the presence of residual organic groups on the sample surface, an FT-IR analysis was performed on the obtained powder. The analysis was performed in the attenuated total reflectance mode with an Avatar 330 spectrometer (Thermo Nicolet, Germany). A minimum of 64 scans with a resolution of 1 cm<sup>-1</sup> was performed. Thermogravimetric measurements were performed in a Netzsch STA 429 CD with a heating rate of 10°C·min<sup>-1</sup> up to 1000 °C in air atmosphere.

Isothermal hysteresis loops of nanopowders obtained after drying the alcoholic suspensions were measured in the temperature interval 10 – 300 K by means of a vibrating sample magnetometer (Lakeshore VSM 7400) operating in the magnetic field range  $-17 \text{ kOe} < H < 17 \text{ kOe}$  equipped with a liquid-He cryostat. Field-cooled (FC) and zero field cooled (ZFC) magnetization curves were measured under a bias field of 100 Oe at a constant temperature sweep rate of approximately 4 K/min.

## 2.4 Preparation of epoxy-magnetite nanocomposites

Epoxy resins containing  $\text{Fe}_3\text{O}_4$  nanoparticles were prepared via cationic polymerization of an aliphatic epoxy resin (bisphenol A diglycidyl ether, DGEBA) in the presence of  $\text{Fe}_3\text{O}_4$  synthesized via NHSG process. The formulations were prepared by adding the alcoholic suspension of magnetite nanoparticles (prepared as previously described) in the range between 0.5 to 4 phr (parts of  $\text{Fe}_3\text{O}_4$  per hundred parts of resins) of actual  $\text{Fe}_3\text{O}_4$  content with respect to the epoxy resin (see composition details in Table 2). A typical formulation was prepared by mixing magnetite suspension and epoxy resin by using a magnetic stirrer (15 min mixing time) and an ultrasonic bath (15 min mixing time). The cationic thermal initiator was added to all the formulations at a concentration equal to 2 phr.

The formulations were cast into silicone moulds having cavities with dimension  $8 \times 1 \times 0.3 \text{ cm}^3$ . All the formulations were cured at  $180^\circ\text{C}$  for 3 hrs.

**Table 2**

Composition of the thermally-curable composite formulations (\*actual magnetite content experimentally determined by thermogravimetric analysis).

Composite code	DGEBA (g)	Yb(OTf) <sub>3</sub> (g)	BzOH (g)	Fe(AcAc) <sub>3</sub> (g)	Fe(AcAc) <sub>3</sub> :BzOH molar ratio	Nominal $\text{Fe}_3\text{O}_4$ (phr/wt%)
C_0				0	0	0
C_05				0.080	0.03	0.5
C_1	3.50	0.12	2.51	0.161	0.06	1.0
C_2				0.323	0.12	2.0
C_4				0.648	0.24	3.8

## 2.5 Characterization of epoxy-magnetite nanocomposites

To obtain the glass transition temperature ( $T_g$ ) of the obtained composites, taken as the mean value of the energy jump of the thermogram (average value between the onset and the endpoint of the glass transition range), differential scanning calorimetry (DSC) was carried out using a Thermal Analysis TA2010 instrument at a scanning rate of  $3^\circ\text{C} \cdot \text{min}^{-1}$  from  $-10^\circ\text{C}$  to  $200^\circ\text{C}$  in  $\text{N}_2$  atmosphere.



The gel content was determined on the cured composites by measuring the weight loss after 24 hrs extraction with chloroform at room temperature according to an adaptation of the standard test method ASTM D 2765-84. FT-IR analysis was performed on the obtained composites to evaluate the epoxy conversion during the thermal curing. The analysis was performed in the same conditions already reported for the powders.

Transmission electron microscopy (TEM) was carried out on nanocomposite samples in order to evaluate the distribution and dispersion of magnetite nanoparticles into epoxy resin and correlate the structural characteristics with the magnetic properties of nanocomposites. TEM analysis was performed on a Tecnai 10 electron microscope (FEI Company, USA), using an accelerating voltage of 100 kV.

Initially the nanocomposite samples were trimmed into a shape of trapezoidal flat pyramid with a glass blade and then sectioned into ultrathin slices (100-150 nm) at -30°C using a cryo-ultramicrotome Leica UC6 (Leica Microsystems, Austria) equipped with a diamond knife (Diatome, USA) working at a knife angle of 35° and with a cutting rate of 300 µm/sec. Sample sections were collected on a 40% v/v dimethylsulfoxide water solution and then deposited on 200 mesh copper grids.

The isothermal magnetization loops of magnetic nanocomposites were measured in the temperature interval 10-300 K by an ultra-sensitive alternating-gradient field magnetometer (AGFM) operating in the field range  $-18 \text{ kOe} < H < 18 \text{ kOe}$  and equipped with a liquid-He continuous flow cryostat.

Field-cooled (FC) and zero field-cooled (ZFC) curves of epoxy samples were obtained through AGFM under the same operating conditions as for the nanopowders.

### **3. Results and Discussion**

#### **3.1 Fe<sub>3</sub>O<sub>4</sub> powders characterization**

##### **3.1.1 Structure, morphology and physico-chemical properties.**

XRD patterns of synthesized powders were reported in Fig. 1, which shows that the powders are composed by magnetite (JCPDS file 01-075-0449) as crystalline phase. In particular the average crystalline size, as determined by Scherrer equation, is around  $9 \pm 1$  nm independently on the Fe(AcAc)<sub>3</sub>:BzOH ratio. However, the broad peaks, commonly observed when the powder has nanometric sizes, did not allow to completely discard the presence of maghemite, as they possess similar structures with comparable cell parameters.

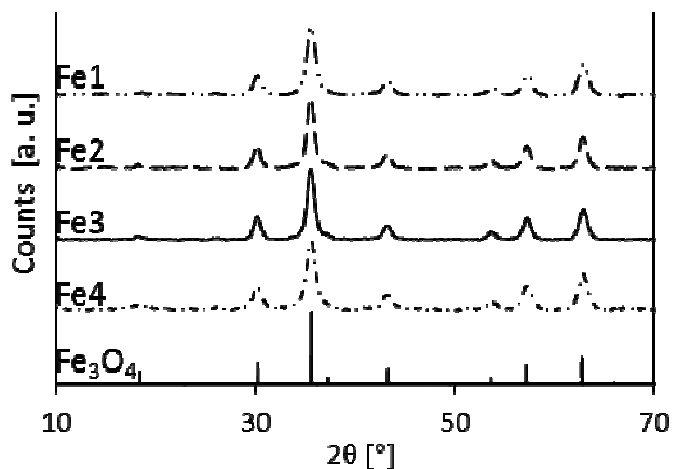


**Fig. 1.** XRD pattern of Fe1, Fe2, Fe3 and Fe4 powders. Magnetite lines are from JCPDS 01-075-0449

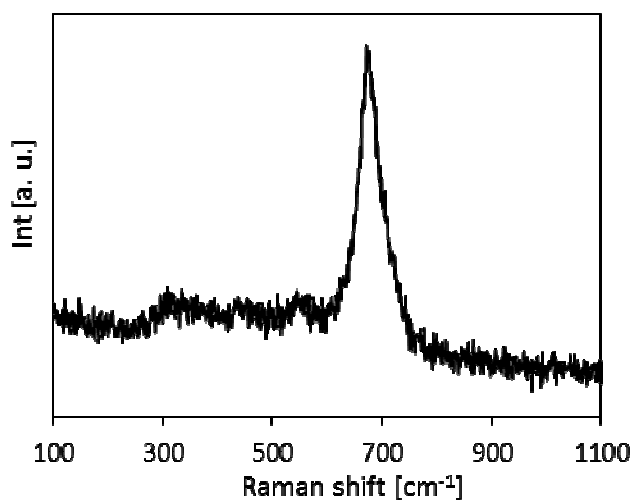


**Fig. 2.** Raman spectrum of magnetite powders synthesized by NHSG process (sample F1 as representative).

Raman spectroscopy allows one to differentiate the iron oxide phases. The Raman spectra of nanoparticles (the spectrum of Fe1 powder shown in Fig. 2 is representative of all samples) exhibit the characteristic bands of magnetite at  $668\text{ cm}^{-1}$  assigned to the  $A_{1g}$  transition [30].

Fig. 3 reports the TEM images of the obtained magnetite particles; these show nanometric crystals with an average particle size that slightly increases as the  $\text{Fe}(\text{AcAc})_3\text{:BzOH}$  ratio is decreased (from  $7.2\pm 0.9\text{ nm}$  to  $10.2\pm 1.7\text{ nm}$ , Table 1) in good agreement with the data obtained by XRD elaboration. The image software analysis showed that the  $\text{Fe}(\text{AcAc})_3\text{:BzOH}$  ratio has a slight influence on the crystal morphology as evidenced by aspect ratio values (Table 1) that slightly increased as the  $\text{Fe}(\text{AcAc})_3\text{:BzOH}$  ratio is increased.

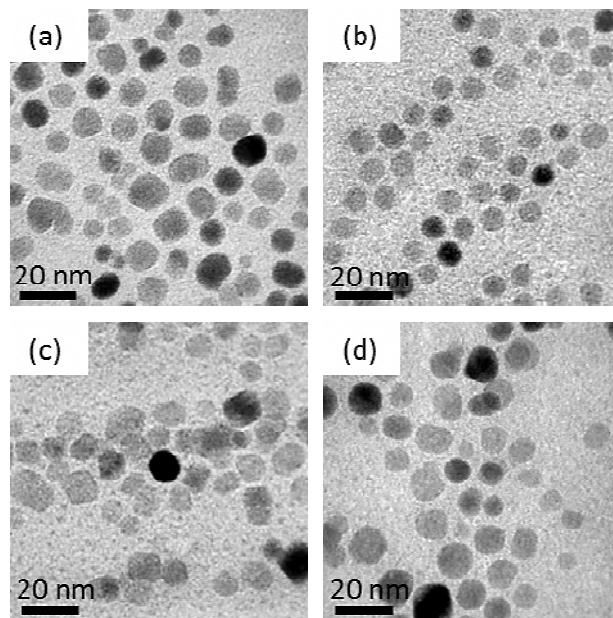


**Fig. 3.** TEM images of Fe1 (a), Fe2 (b), Fe3 (c) and Fe4 (d) powders, synthesized by NHSG process.

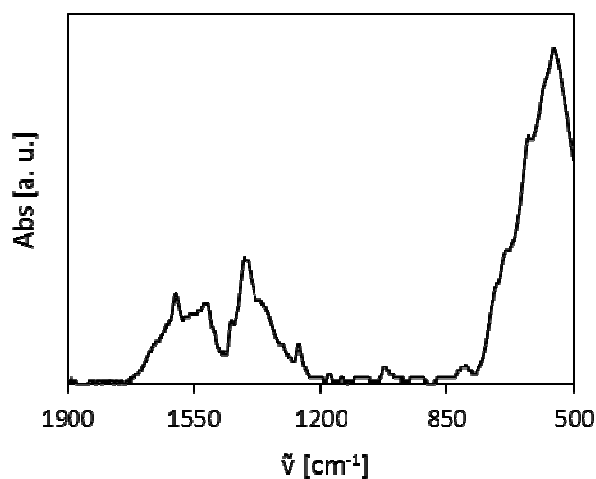


**Fig. 4.** IR spectra of magnetite powders synthesized by NHSG process (sample F1 as representative).

Moreover the crystals are characterized by a good dispersion and low degree of agglomeration.

Thermogravimetric analysis (not reported here) evidences the presence of organic groups on the magnetite particles surface showing a well-defined mass loss profile over a temperature range of 200-450 °C attributed to the decomposition of the organic ligands.

The presence of organic ligand on the particle surface was confirmed by FT-IR analysis. Fig. 4 shows a typical infrared spectrum of magnetite nanopowders. In particular the adsorption at 540  $\text{cm}^{-1}$  can be assigned to the Fe-O bond [31] while the other adsorptions are compatible with the presence on the particles surfaces of carboxylic groups, in particular benzoate [32], probably present due to the oxidation of BzOH to benzoic acid caused by the reduction of  $\text{Fe}^{3+}$  to  $\text{Fe}^{2+}$ .

In fact, the absorptions at  $1520\text{ cm}^{-1}$  and  $1400\text{ cm}^{-1}$  can be assigned to symmetric and asymmetric stretch of the carboxylate group while the absorptions at  $1450\text{ cm}^{-1}$  and  $1600\text{ cm}^{-1}$  can be assigned to the to the C=C stretch in the phenyl group.

### 3.1.2 Magnetic properties.

The high-field magnetization at  $T = 10\text{ K}$ , which is close to the maximum saturation magnetization  $M_s$  is reported in Table 3 for all dried magnetite nanopowders (Fe1 to Fe4). The values are definitely lower than in bulk magnetite ( $98\text{ emu g}^{-1}$  at  $10\text{ K}$ ) [33] and slightly dependent on BzOH content, although no definite trend is observed. The present values are in good agreement with the literature data for magnetite nanoparticles of similar size [34,35]. The small differences among nanopowders can be related to a different amount of magnetically disordered states at the surface of each nanoparticle [34,36].

The FC/ZFC curves of the nanopowders are shown in Fig. 5a. In order to make the comparison among signals of different amplitude easier, each curve was normalized to the value at  $T = 300\text{ K}$ . All FC curves are almost flat and all ZFC curves exhibit a broad maximum immediately before merging with the

**Table 3**

Temperature of the maximum of the ZFC curve ( $T_M$ ), coercive field at  $T = 10\text{ K}$  ( $H_c, 10K$ ); saturation magnetization at  $T = 10\text{ K}$  ( $M_s, 10K$ ); average nanoparticle size obtained from  $T_M$  using for Keff the value of bulk magnetite ( $D^*_{ave}$ ); average nanoparticle size obtained from  $T_M$  using for Keff the values reported in Fig. 6 ( $D_{ave}$ ).

Sample	$T_M$ (K)	$H_c, 10K$ (Oe)	$M_s, 10K$ (emu/g)	$D^*_{ave}$ from $T_M$ (nm)	$D_{ave}$ from $T_M$ (nm)
Fe1	140	133	61.4	15.5	-
Fe2	215	199	65.2	17.8	-
Fe3	265	200	65.1	19.1	-
Fe4	170	115	58.8	16.5	-
C_05	48	166	44.1	10.8	9.3
C_1	37	191	-	9.9	10.0
C_2	61	249	50.7	11.7	12.4
C_4	58	431	37.6	11.5	12.9

corresponding FC curve; the temperature of the maximum ( $T_M$ ), shown in Table 3, does not linearly increase with increasing BzOH content.

The coercive fields  $H_c$  of the isothermal hysteresis loops of dried nanopowders are shown in Fig. 6a as functions of temperature. All curves monotonously increase with decreasing temperature; the  $H_c$  values at  $T = 10\text{ K}$  are reported in Table 3. In all samples, and particularly in samples Fe2 and Fe3, magnetic hysteresis does not entirely disappear up to high temperature (above  $200\text{ K}$ ).

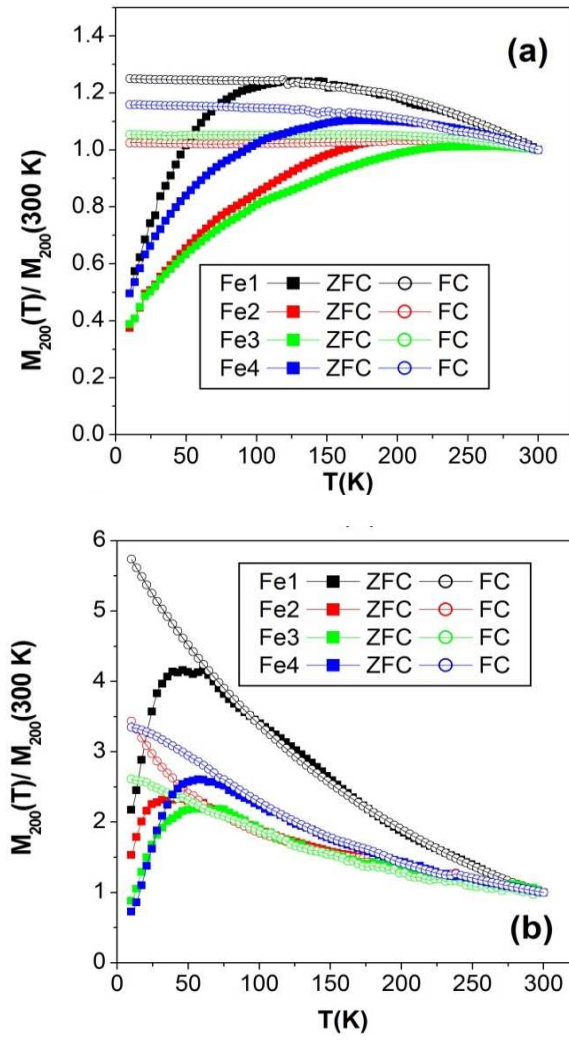


**Fig. 5.** Normalized ZFC and FC magnetization curves of dried nanopowders (panel (a)) and epoxy nanocomposites (panel (b))

## 3.2 Epoxy-magnetite nanocomposite characterization

### 3.2.1 Structure, morphology and physico-chemical properties.

Gel content and glass transition temperature values determined after curing of composites are reported in Table 4.

**Table 4**  
Gel content (G), epoxy conversion ( $c_{\text{epoxy}}$ ) and glass transition temperature ( $T_g$ ) of prepared composites

Composite code	G (%)	$c_{\text{epoxy}}$ (%)	$T_g$ (°C)
C_05	58	89	30.2
C_1	33	89	29.9
C_2	14	90	37.7
C_4	13	90	41.6

The extractable/soluble fraction, corresponding to (1-G), could be related to the molecules of DGEBA, BzOH and other by-products of the NHSG process which are not covalently linked to the three-dimensional network after curing/cross-linking reactions. The values of G decrease significantly by increasing the amount of  $\text{Fe}(\text{AcAc})_3$  precursor in the thermally-curable formulation and correspondingly the final amount of magnetite. In this respect, gel content analysis suggests that the by-products of the reaction between  $\text{Fe}(\text{AcAc})_3$  and BzOH limit the formation of a fully developed three-dimensional network according to the proposed ‘activated monomer’ mechanism during the propagation step in the cationic ring-opening epoxy polymerization. This hypothesis is supported by considering that the epoxy groups conversion (determined by FT-IR analysis according to the decrement of the peak centred at  $914\text{ cm}^{-1}$  corresponding to the asymmetric stretching of oxirane ring) is relatively high and almost equal (89-90%) for all the composite materials suggesting that the ring-opening reaction was not affected by the presence of the by-products of the reaction between  $\text{Fe}(\text{AcAc})_3$  and BzOH.

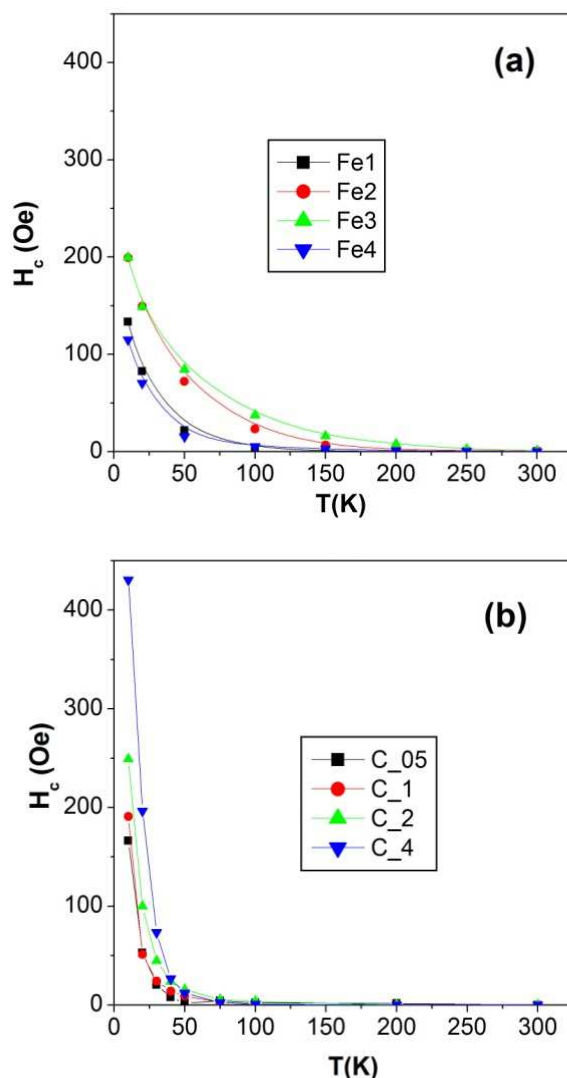


**Fig. 6.** Coercive field as a function of temperature in dried nanopowders (panel (a)) and epoxy nanocomposites (panel (b))

Concerning DSC analysis, a decrement of  $T_g$  is usually expected by decreasing the crosslinking density of a three-dimensional network. In the present case the opposite trend was been observed with  $T_g$  values that monotonically increase from a minimum of 12.4 °C for C\_0 (reference material without magnetite filler) to a maximum of 41.6 °C for C\_4 (composite with the lowest gel content, and thus crosslinking density, and the highest content of magnetite filler). The observed behaviour could be explained as a hydrodynamic effect taking into account that, in the case of polymers filled with particles, the incorporation of rigid fillers into a polymeric matrix made difficult the movement of the polymer chains leading to a shift of  $T_g$  values to higher temperatures (stiffening effect due to a constrained chain mobility by well-dispersed fillers).

TEM images of magnetite-containing composites are reported in Fig. 7. An unforeseen morphology can be observed by TEM analysis taking into account that an increase of the tendency to particle aggregation is usually expected by increasing the concentration of dispersed particles. On the contrary, in the present case aggregation phenomena are clearly evident only in the case of low content of magnetite in the composite (C\_05 and C\_1). Quite surprisingly, a very good distribution and dispersion state of magnetite nanoparticles with the polymer matrix can be observed for the sample with the highest filler content (C\_4). This behaviour could be ascribed to the formation of a particle surface chemically with a relatively low surface tension and high compatibility with the surrounding organic matrix which is able to minimize particle-particle interactions.

### **3.2.2 Magnetic properties.**

The saturation magnetization (per gram of  $\text{Fe}_3\text{O}_4$ ) of the nanocomposites (C\_05 to C\_4, with the exclusion of sample C\_1 where the total mass was too small to obtain a reliable value) is systematically lower than in the corresponding nanopowders. This can be related to an enhancement of the surface magnetic disorder at the nanoparticle-resin interface, as already observed by other groups [37-39]; however, our experimental methods do not allow for a deeper study of this effect.

The normalized FC/ZFC curves are shown in Fig. 5b. In this case, the experimental data are more scattered owing to the smaller amplitude of the magnetic signals.

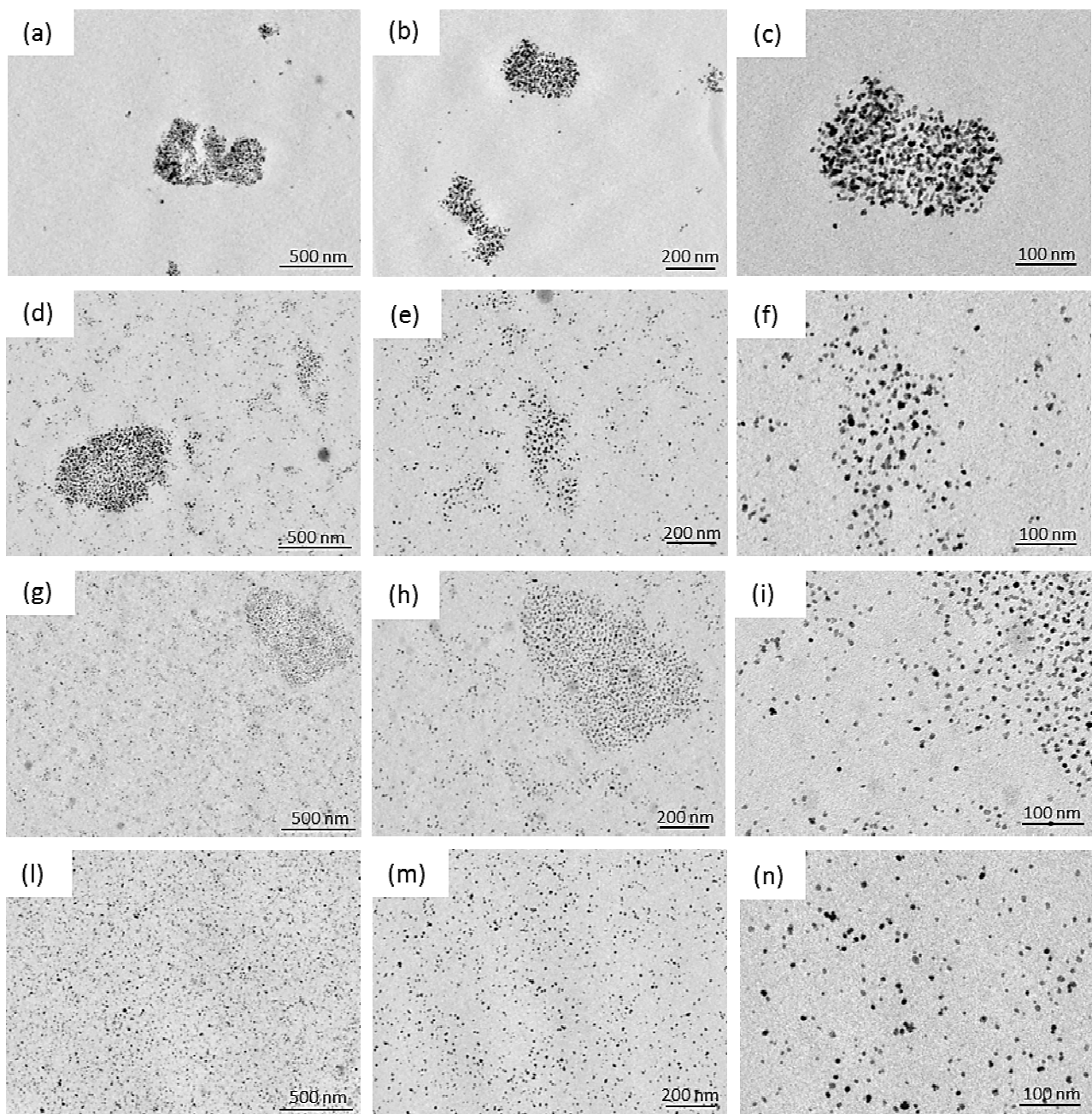


**Fig. 7.** TEM images of C\_05 (a-c), C\_1 (d-f), C\_2 (g-i) and C\_4 (l-n) nanocomposites, prepared by in-situ approach, at different magnifications



All curves exhibit a steeper and sharper behavior than the corresponding nanopowders, the maximum of the ZFC curve being displaced towards lower temperatures and occurring just below the temperature where the ZFC and FC curves merge into each other; the measured  $T_M$  values are reported in Table 3. The FC curves steadily decrease with increasing temperature.

The coercive fields  $H_c$  of nanocomposites are shown in Fig. 6b. This quantity monotonously increases with decreasing temperature, a substantial enhancement of the coercive field being observed with respect to the corresponding nanopowders; the  $H_c$  values at  $T = 10$  K are reported in Table 3 and increase with increasing NP concentration in the host polymer. In all samples the coercive field rapidly drops with temperature and finally disappears just above 100 K.

### 3.3 Nanoparticle average size and size distribution in nanocomposites

The changes observed in the shape of the FC/ZFC curves between the two sets of samples (nanopowders and nanocomposites) indicate that a significant degree of NP aggregation is present in the dried powders. In fact, the maximum of the ZFC curves of a nanoparticle system gives an estimate of the average NP size  $D_{ave}$  through the following relation:

$$D_{ave}^* \cong \left( \frac{6}{\pi} \frac{25 k_B T_M}{|K_{eff}|} \right)^{1/3} \quad (1)$$

where it is assumed that the a nanoparticle of volume  $V$  has a spherical shape,  $D_{ave}^*$  being the effective NP diameter, and use is made of the well-known relation  $T_M \cong 25 k_B V / |K_{eff}|$  [40]. Assuming  $|K_{eff}| \cong 2.5 \times 10^5$  erg/cm<sup>3</sup> at low temperatures (this is the measured value of the anisotropy constant  $K_1$  in bulk magnetite [41] and can be a good starting estimate for  $K_{eff}$  in the present materials containing nearly spherical NPs), one gets the  $D_{ave}^*$  values reported in Table 3. The estimates are in contrast with direct evidence from TEM observation (Table 1). This suggests that the magnetic units individually responding to the magnetic field are typically comprised of some nanoparticles in these powders,  $D_{ave}$  being in this case rather an effective magnetic size of a NP cluster than the true size of a single nanoparticle. The degree of aggregation of the nanopowders as measured by  $T_M$  is somewhat influenced by the amount of BzOH used during preparation. The Fe<sub>4</sub> material, used to produce the C<sub>4</sub> nanocomposite with an excellent dispersibility of nanoparticles (see Fig. 7), already exhibits a lower degree of aggregation in powder form.

On the other hand, the degree of aggregation of nanoparticles in magnetic nanocomposites is significantly lower, as indicated by the magnetic size  $D_{ave}$  evaluated from Eq. 1, which is closer to the size given by TEM images, although still systematically higher (Table 3). This indicates a process of nanoparticle disaggregation when entering the nanocomposite. A similar effect was found e.g. in magnetic inks containing aggregate magnetite nanopowders which became more independent after spraying on a flat surface [42]; in that case, the kinetic energy introduced by the ejection technique was able to break most of the electrostatic or magnetic bonds among nanoparticles,

making their response more individual; in the present case the proposed innovative synthesis has a similar effect of disaggregation, as indeed observed for magnetite nanoparticles prepared with a different method and dissolved in a different epoxy resin [28].

The magnetic size estimated from the maximum of the ZFC curve would seem to suggest some extant degree of NP aggregation even in the epoxy resins (compare Tables 1 and 3); however, TEM images (Fig. 7) show that magnetite nanoparticles are basically not aggregate in all composites, even if large deviations from uniform distribution are observed in some samples such as C\_05 and C\_1.

The difference between the estimate through Eq. 1 and the actual NP size could therefore be ascribed to an inadequate choice of the effective anisotropy constant  $K_{eff}$ , which is actually difficult to estimate in nanoparticulate systems where significant surface effects can be present [43]. Instead, shape anisotropy plays a rather negligible role in nanoparticles characterized by an aspect ratio close to one (see Table 1). In order to remove the difficulty arising from the unknown value of  $K_{eff}$ , a different method is exploited here to derive both the average NP size and the NP size distribution from a deeper analysis of the FC/ZFC curves [44].

The distribution of blocking temperatures  $p(T_B)$  of a NP system can be obtained from the temperature derivative of the difference  $\Delta(T)$  between ZFC and FC magnetization curves [44]. This quantity is closely proportional to the  $p(T_B)$  when the intrinsic temperature dependence of the NP magnetic moments can be neglected [44], a condition fulfilled from 0 K to 300 K in these samples, as indicated by the  $M_s(T)$  behavior. Explicitly:

$$p(T_B) \cong - \left. \frac{d\Delta(T)}{dT} \right|_{T=T_B} \quad (2)$$

From the  $p(T_B)$  functions one can derive the corresponding distribution  $p(D)$  of NP sizes through the relations:

$$\begin{cases} p(D)dD = p(T_B)dT_B \\ D = \left( \frac{6}{\pi} \frac{25k_B}{|K_{eff}|} T_B \right)^{1/3} \end{cases} \quad (3)$$

As a consequence, the  $p(D)$  function is univocally linked to the  $p(T_B)$  function by:

$$p(D) = \frac{\pi |K_{eff}|}{2 \cdot 25k_B} D^2 p(T_B \rightarrow D) \quad (4)$$

The  $p(D)$  curves obtained applying such a procedure are shown in Fig. 8 for all nanocomposite samples. All curves

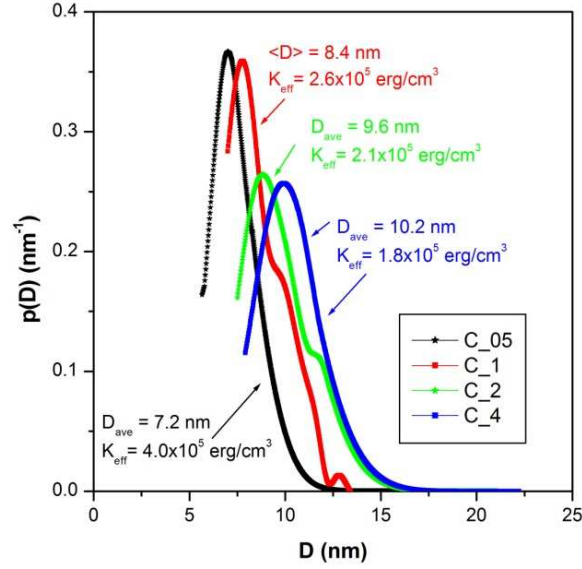


**Fig. 8.** Size distribution functions of nanoparticles embedded in epoxy resins, as determined from Eqs. (2)-(4)

were slightly smoothed in order to damp oscillations of unphysical nature related to the process of numerical differentiation. It should be noted that the  $p(D)$  curves obtained by this method are necessarily incomplete on the low- $D$  side; they have been normalized in such a way that the area of the portion of plane between each curve and the horizontal axis is the same. The distribution functions are basically symmetric around the mode, in some cases with small bumps which can be related to the presence of minor peaks at higher size values. The standard deviation of NP sizes from the mode of the distribution function is rather limited and fully compatible with the natural spread of sizes for the magnetite NPs obtained by the present preparation route (see Table 1).

It should be explicitly noted that the position along the horizontal axis of the  $p(D)$  function depends on the choice of the effective anisotropy constant of nanoparticles,  $|K_{eff}|$ . This provides a way to determine this quantity.

In fact, the parameter  $|K_{eff}|$  can be obtained for each studied material by requiring that the average NP size obtained as  $D_{ave} = \int Dp(D)dD$  be equal to the result of TEM observations. The  $|K_{eff}|$  values needed to obtain such a match are reported in Fig. 8 for each curve. Note that the analysis allows one to determine the magnitude of  $K_{eff}$  but not its sign which could be either positive or negative (it should be recalled that in bulk magnetite the first magnetocrystalline anisotropy constant is a negative quantity [41]). The deviation of the  $|K_{eff}|$  values reported in Fig. 8 and the low-temperature crystal anisotropy of bulk magnetite indicates that a surface contribution exists. An estimate of the surface anisotropy constant  $K_s$  is obtained by fitting the experimental  $K_{eff}$  values to the expression [43]:

$$K_{eff} = K_{\infty} + \frac{6K_s}{D_{ave}} \quad (5)$$

where  $K_\infty$  is the anisotropy constant for the bulk material ( $D_{ave} \rightarrow \infty$ ), taken equal to  $-2.5 \times 10^5$  erg/cm<sup>3</sup>. The experimental data (Fig. 9a) are in good agreement with Eq. (5); the value  $K_s = +7.5 \times 10^{-2}$  erg/cm<sup>2</sup> is obtained from the fit. This indicates that the surface anisotropy is opposite in sign to the volume anisotropy; the total  $K_{eff}$  is a positive quantity. A positive  $K_s$  is indeed expected by different models of surface anisotropy [45]. Our estimate for  $K_s$  is in agreement with published data for iron oxide NPs (size: 7.8 nm), where the measured  $K_{eff}$  yields a  $K_s$  value equal to either  $7 \times 10^{-2}$  or  $14 \times 10^{-2}$  erg/cm<sup>2</sup> (depending on the sign of  $K_{eff}$ , which was not determined in that case) [34].

Once a reliable  $|K_{eff}|$  value was determined for each sample, Eq. (1) can be again used, providing a better estimate of  $D_{ave}$  on the basis of the measured  $T_M$  values. The results are reported in Fig.9b (open circles) where they are compared to the sizes obtained from TEM observations (open squares) and from the p(D) curve analysis (asterisks); the latter two datasets being of course identical because of the procedure we have followed. Even when more accurate  $|K_{eff}|$  values are used, the sizes estimated from the maxima of the ZFC curves are systematically higher by 20-30% than the real values. The discrepancy is presumably related to the presence of a finite spread of NP sizes, while Eq. (1) should be applied to ideally monodisperse NPs.

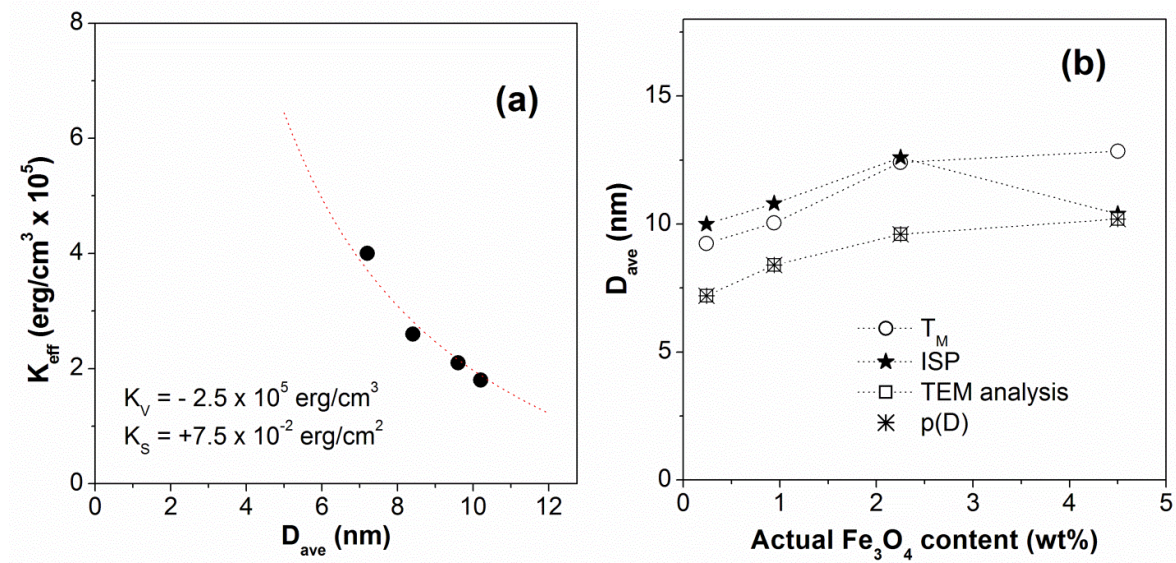


**Fig. 9.** Panel (a): Effective anisotropy constants of magnetic nanoparticles in epoxy resins as functions of NP size; panel (b): Nanoparticle size in nanocomposites with a different magnetite content, as determined by different techniques (see text for details)

### 3.4 Magnetic nanocomposites as interacting superparamagnets in the ISP model

The ISP model [27] has been developed to deal with weak but non negligible effects of dipolar magnetic interaction at intermediate to high temperatures in systems containing magnetic NPs. Dipolar interaction effects among NPs can be the source of frustration of moments and of frozen magnetically disordered states at very low temperatures [26]; well above blocking temperature they manifest themselves in the form of departures from the standard SP scaling law [23].

The ISP model is applied to temperatures where the dipolar interaction energy, although no longer being dominant as at very low  $T$  [26] is nevertheless still comparable in magnitude to the thermal energy  $k_B T$ . When dipolar interaction is weak a mean-field approach such as the ISP model can be used [46].

The ISP-model prediction for the isothermal anhysteretic magnetization of a monodisperse NP system containing  $N$  weakly interacting magnetic moments  $\mu$  is [46]:

$$M_{ISP} = N\mu L\left[\frac{\mu H}{k_B(T + T^*)}\right] = M_s L\left[\frac{M_s H}{Nk_B T + \alpha M_s^2}\right] \quad (6)$$

where  $L$  is the Langevin function and the term  $K_B T^* = \alpha \mu^2 / d^3 = \alpha N \mu^2 = \alpha M_s^2 / N$  at the denominator of the Langevin function's argument depicts the dipolar energy,  $\alpha$  being a number close to unity;  $N$  the number of nanoparticles per unit volume. The model is straightforwardly extended to the case of a distribution of NP sizes. Recently the role of the effective interaction temperature  $T^*$  and its occurrence at the denominator of the argument of the Langevin function have been placed on a firm physical basis [47].

A central quantity in the model is the ratio of r.m.s. dipolar interaction energy to thermal energy, i.e., the ratio  $T^*/T$ . When  $T^*$  is much smaller than  $T$ , the main source of magnetic disorder are thermal random torques acting on independent magnetic moments, resulting in the standard superparamagnetic (SP) regime. Instead, when  $T^*$  is larger than  $T$  a significant fluctuating dipolar energy adds to the thermal energy contributing to enhance the disorder of magnetic moments [47].

Analysis of data using the ISP model (not reported here; the reader may refer to Refs. 27 and 46-47) allows one to obtain the  $T^*$  values from experimental data. The ratio  $T^*/T$  plotted as a function of temperature allows one to draw a diagram of the different magnetic regimes experienced above blocking by weakly interacting magnetic NP systems. The  $T^*/T$  curves are shown in Fig. 10 for all nanocomposites. The dotted horizontal lines mark the changes of magnetic regime; in particular, the ISP regime approximately extends in the interval  $1 \leq T^*/T \leq 25$  [27]. A higher / lower vertical position of the  $T^*/T$  curve corresponds to higher / lower amount of r.m.s. dipolar energy. The results shown in Fig. 10 indicate that this energy is not a monotonic function of the NP concentration in the nanocomposites, the lowest curve belonging to the magnetically most concentrated sample (C\_4). This is sort of an unexpected result; in fact  $T^*$  is proportional to the quantity  $\mu^2/d^3$  where  $\mu$  is the average magnetic moment per nanoparticle and  $d$  the average interparticle distance. In turn,  $d$  is proportional to  $N^{-1/3}$ ,  $N$  being the volume concentration of magnetic NPs. Therefore,  $T^* \approx N \mu^2$  and one would therefore expect that the higher the concentration, the higher the effective interaction temperature  $T^*$ , which is contradicted by the experimental evidence of Fig. 10.

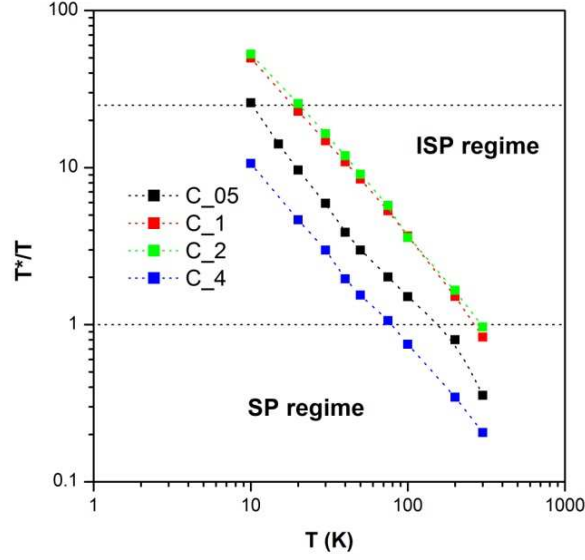


**Fig. 10.**  $T^*/T$  ratio of the ISP model as a function of temperature in all nanocomposites

This discrepancy can be understood considering that in some of the studied composites the distribution of nanoparticles is far from being uniform, as evidenced by TEM images. In fact, the most uniform NP distribution occurs in the C\_4 sample. Now, if the NP distribution is non-uniform, the overall dipolar energy of the NP system increases.

The following simple argument can be provided. Let us suppose that the magnetic nanoparticles do not occupy the entire volume  $V$  of a sample, being instead concentrated in a smaller volume  $\beta V$  (with  $\beta < 1$ ). Of course, the volume  $\beta V$  is the sum of the volumes of individual “islands” of high NP density as those observed, e.g., in sample C\_05 (see Fig. 7). While for a uniform distribution of nanoparticles the interparticle distance would be  $d = N^{-1/3}$ , within each island the distance decreases to  $d'' = (N/\beta)^{-1/3} = d\beta^{1/3}$  and the effective temperature increases to  $T^* = T^*/\beta$ . Such an argument, albeit oversimplified, helps understanding why the  $T^*/T$  curve is lower in the C\_4 sample where the uniformity of nanoparticles is much better, in spite of the larger number of magnetite NPs present there: the increase in  $N$  with respect to sample C\_05 is more than compensated by the increase in  $\beta$  (which is equal to 1 in nanocomposite C\_4), leading to a larger interparticle distance. Instead, in the C\_05 sample, where  $\beta \ll 1$  (see Fig. 7) the nanoparticles in the islands are much closer to each other and more interacting, even if their overall number per unit volume is lower than in sample C\_4.

The same argument can be used to understand the behavior of the size predicted by the ISP model, shown in Fig. 9 (full stars). In fact, a uniform distribution of nanoparticles is implicitly assumed by the model. When this condition is fulfilled, such as in sample C\_4, the size predicted by the ISP is in excellent agreement with the TEM value. When this is not the case, however, the size estimated by the ISP model is systematically larger than the true value, because in the presence of concentration

fluctuations the interparticle distance within islands is shorter than expected. By requiring that  $\mu_{ISP}^2/d_{ISP}^3 = \mu_{TEM}^2/d_{TEM}^3$  where  $d_{ISP} = d$  and  $d_{TEM} = d'$ , and keeping in mind that  $\mu_{TEM/ISP} \approx D_{TEM/ISP}^3$ , one gets  $D_{ISP} = D_{TEM}/\beta^{1/6}$ , i.e., the ISP model predicts a larger-than-real value,  $\beta$  being a number less than 1.

Finally, according to the ISP model the argument of the Langevin function (or their superposition when the NPs are polydisperse) is  $y = M_s H / (N k_B T + \alpha M_s^2)$ , which reduces to  $H/M_s$  when the dipolar interaction dominates over the randomizing effect of temperature, i.e. when  $\alpha M_s^2 \gg N k_B T$  [27].

It is therefore possible to envisage a scaling law specific for ISP

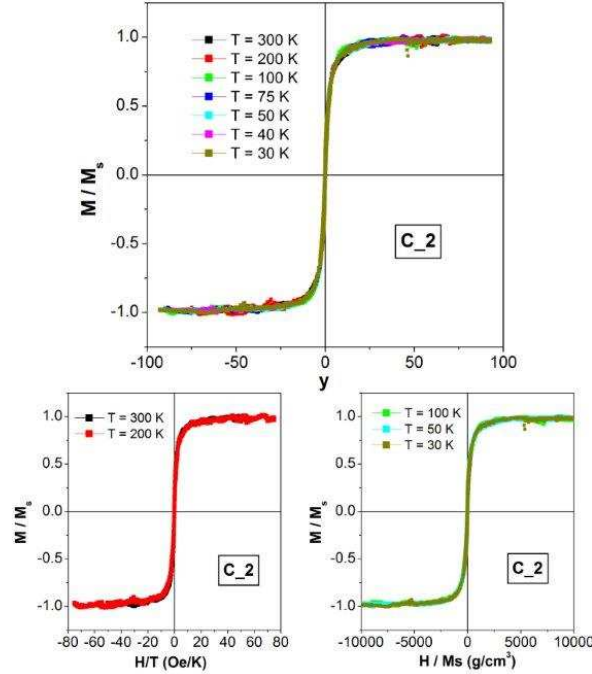


**Fig. 11.** Scaling laws of reduced magnetization in C\_2 nanocomposite. Left: full ISP scaling; Top right: standard SP scaling at high temperatures; Bottom right: simplified ISP scaling at low temperatures

systems and different from the one usually applied to superparamagnetic nanoparticles. As an example, the reduced magnetization curves of sample C\_2 (characterized by the highest  $T^*/T$  values) are reported in Fig. 11 as functions of  $y$  for each measurement temperature. All curves are perfectly superimposed over a remarkably wide temperature range, indicating a perfect agreement with the ISP-model prediction. Note that the quantity  $y$  does not contain free or adjustable parameters, because  $M_s(T)$ ,  $N$ ,  $\alpha$  are univocally determined by experiment and the ISP analysis of the experimental data [27]. It is interesting to further note that for  $T > 200$  K the standard SP scaling law is observed ( $y$  reducing in this case to  $const. \times H/T$ ), while for  $T < 100$  K a simpler ISP scaling law holds ( $y$  reducing in this case to  $const. \times H/M_s$ ). A similar scaling behaviour has been observed in all nanocomposites and is in agreement with experimental data obtained by different groups on other NP systems [48,49].

#### 4. Conclusions

Suspensions of magnetite nanoparticles in benzyl alcohol were synthesized by non-hydrolytic sol-gel (NHSG) process, mixed with an aliphatic epoxy resin and subsequently polymerized in the presence of a cationic thermo-initiator. The chosen strategy allows to obtain a homogeneous composite material being the inorganic particles homogeneously dispersed within the polymeric matrix as indicated by TEM analysis.

The dried nanopowders display a saturation magnetization close to the one observed in a number of similar nanoparticle systems, indicating that some magnetic disorder must be present at the surface; the ZFC/FC curves clearly show that the nanoparticles in the powders are considerably aggregate in spite of the presence of organic ligands at their surfaces. This is confirmed by the temperature dependence of the hysteretic properties too. On the other hand, the magnetic nanocomposites are characterized by a saturation magnetization (per gram of magnetic substance) remarkably lower than the corresponding nanopowders, suggesting that the iron oxide–resin interface plays a role in inducing a higher magnetic disorder at the nanoparticle surface. The FC/ZFC curves indicate that the degree of nanoparticle aggregation is significantly decreased by inclusion in the resin, in agreement with TEM observations. In fact, the behaviour of the coercive field is much closer to what expected from a system of individual nanoparticles.

The distribution of nanoparticle sizes has been determined by operating on the difference between FC and ZFC curves of the nanocomposites, and found to be in good agreement with structural data; a comparison between the results of TEM image analysis and the outcome of the proposed procedure has allowed us to get a reliable estimate of the effective anisotropy constant of the nanoparticles; in turn, the latter has been used to evaluate the surface anisotropy constant, which turns out to be a positive quantity.

The magnetic nanoparticles embedded in the resin cannot be described as being in the ideal superparamagnetic state. Magnetic dipolar interaction is expected to be present even in dilute nanoparticle systems, giving rise to specific effects on magnetization which are revealed by the ISP model. In particular, the reduced magnetization of all nanocomposites closely follows the scaling law predicted by the ISP model, which reduces to the standard superparamagnetic scaling law at high temperatures.

However, the intensity of the magnetic interaction, as measured by the effective temperature  $T^*$ , does not increase linearly with the magnetite content in the resins because of the large fluctuations in nanoparticle volume density evidenced by TEM observations in some samples, giving rise to denser islands comprised of a large number of nanoparticles where the dipolar interaction is locally enhanced.



## Acknowledgements

The authors thank Ing. Laura Ciarcià for her support to the experimental procedure.

## References

- [1] Sanchez C, Belleville P, Popall M, Nicole L. Chem. Soc. Rev., 2011; 40:696-753 DOI: 10.1039/c0cs00136h.
- [2] Fu SY, Feng XQ, Lauke B, Mai Y-W. Composites: Part B, 2008; 39:933-961; DOI: 10.1016/j.compositesb.2008.01.002
- [3] Hanemann T, Szabó DV. Materials, 2010; 3:3468-3517; DOI:10.3390/ma3063468
- [4] Long YZ, Chen ZJ, Duvail JL, Zhang ZM, Wan MX., Physica B, 2005; 370:121-130; DOI: 10.1016/j.physb.2005.09.009
- [5] Godovsky DY. Adv. Polym. Sci., 2000; 153:163-205; DOI: 10.1007/3-540-46414-X\_4
- [6] Oh JK, Park JM. Progress in Polymer Science, 2011; 36:168-189; DOI: 10.1016/j.progpolymsci.2010.08.005
- [7] Massart R. IEEE Trans. Magn., 1981; 17:1247-1248 ; DOI: 10.1109/TMAG.1981.1061188
- [8] Gass J, Poddar P, Almand J, Srinath S, Srikanth H. Adv. Funct. Mater., 2006; 16:71-75; DOI: 10.1002/adfm.200500335
- [9] Gyergyek S, Huskić M, Makovec D, Drofenik M. Colloids and Surfaces A: Physicochem. Eng. Aspects, 2008; 317:49-55; DOI: 10.1016/j.colsurfa.2007.09.035
- [10] González M, Martín-Fabiani I, Baselga J, Pozuelo J. Materials Chemistry and Physics, 2012; 132:618-624; DOI: 10.1016/j.matchemphys.2011.11.077
- [11] Guo J, Zhang X, Gu H, Wang Y, Yan X, Ding D, Long J, Tadakamalla S, Wang Q, Khan MA, Liu J, Zhang X, Weeks BL, Sun L, Young DP, Wei S, Guo Z. RSC Adv., 2014; 4:36560-36572; DOI: 10.1039/C4RA07359B

- [12] Sanchez C, Julian B, Belleville P, Popall M. J. Mater. Chem., 2005; 15:3559-3592; DOI: 10.1039/B509097K
- [13] Florini N, Barrera G, Allia P, Tiberto P, Bondioli F. J. Am. Ceram. Soc., 2013; 96:3169-3175; DOI: 10.1111/jace.12469
- [14] Bourget L, Corriu RJP, Leclercq D, Mutin PH, Vioux A. J. Non-Cryst. Solids, 1998;242:81-91;
- [15] Niederberger M, Garnweitner G, Pinna N, Neri G. Prog. Solid State Ch., 2005; 33:59-70; DOI: 10.1016/j.progsolidstchem.2005.11.032
- [16] Pinna N, Garnweitner G, Antonietti M, . Niederberger M. Adv. Mater., 2004; 16:2196-2200; DOI: 10.1002/adma.200400460
- [17] Mutin PH, Vioux A. Chem. Mater., 2009; 21:582-596; DOI: 10.1021/cm802348c
- [18] Morselli D, Messori M, Bondioli F. J. Mater. Sci., 2011; 46:6609-6617; DOI: 10.1007/s10853-011-5610-9
- [19] Morselli D, Bondioli F, Fiorini M, Messori M. J. Mater. Sci., 2012; 47:7003-7012; DOI: 10.1007/s10853-012-6651-4
- [20] Morselli D, Bondioli F, Sangermano M, Messori M. Polymer, 2012; 53:283-290; DOI: 10.1016/j.polymer.2011.12.006
- [21] Hay JN, Raval HM. Chem. Mater., 2001; 13:3396-3403;
- [22] Laurent S, Forge D, Port M, Roch A, Robic C, Elst LV, Muller RN. Chem. Rev., 2008; 108:2064-2110; DOI: 10.1021/cr068445e.
- [23] Nardi T, Sangermano M, Leterrier Y, Allia P, Tiberto P, Månson JAE. Polymer, 2013; 54:4472-4479; DOI: 10.1016/j.polymer.2013.06.052
- [24] Nardi T, Leterrier Y, Karimi A, Månson JAE. RSC Adv., 2014; 4:7246-7255; DOI: 10.1002/polb.23443
- [25] Sen T, Shimpi NG, Mishra S, Sharma R. Sensors and Actuators B, 2014; 190:120- 126; DOI: 10.1016/j.snb.2013.07.091

- [26] Fiorani D, Peddis D. J. Phys.: Conf. Series, 2014; 521:012006:1-012006-9; DOI: 10.1088/1742-6596/521/1/012006
- [27] Allia P, Coisson M, Tiberto P, Vinai F, Knobel M, Novak MA, Nunes WC. Phys. Rev. B, 2001; DOI: 64:144420-144431;
- [28] Sangermano M, Allia P, Tiberto P, Barrera G, Bondioli F, Florini N, Messori M. Macrom. Chem and Phys., 2013; 214:508-516; DOI: 10.1002/macp.201200494
- [29] Langford JJ, Wilson AJC, J. Appl. Crystallogr., 1978; 11:102-113
- [30] Daou T, Pourroy G, Begin-Colin S, Greneche J, Ulhaq-Bouillet C, Legare P, Bernhardt P, Leuvrey C, Rogez G. Chemistry of Materials, 2006; 18:4399-4404; DOI: 10.1021/cm060805r
- [31] Goncalves RH, Cardoso CA, Leite ER. J. Mat. Chem., 2010; 20:1167-1172; DOI: 10.139/b917030h
- [32] Lewandowski W, Barańska H. Vib. Spectr., 1991; 2:211-220; DOI: 10.1016/0924-2031(91)85028-L
- [33] Cullity BD, Graham CD, Introduction to Magnetic Materials, IEEE Press – Wiley, Piscataway, NJ USA, 2nd edn., 2009.
- [34] Lin CR, Chiang RK, Wang JS, Sung TW. J. Appl. Phys., 2006; 99:08N710; DOI: 10.1063/1.2172891
- [35] Allia P, Tiberto P, Coisson M, Chiolerio A, Celegato F, Vinai F, Sangermano M, Suber L, Marchegiani G. J. Nanopart. Res., 2011; 13:5615-5626; DOI: 10.1007/s1 1051-011-0249-7
- [36] Berkowitz AE, Kodama RH, Makhlof SA, Parker FT, Spada FE, McNiff Jr. EJ, Foner S. J. Magn. Mater., 1999; 196-197:591-594; DOI: 10.1016/S0304-8853(98)00845-2
- [37] Cui L, Gu H, Xu H, Shi D. Mater. Lett., 2006; 60:2929-2932; DOI: 10.1007/12\_2010\_59
- [38] Yang J., Park SB, Yoon HG, Huh YM, Haam S. Int. J. Pharmaceutics, 2006; 324:185-190; DOI: 10.1016/j.ijpharm.2006.06.029
- [39] Bhatt AS, Bhat DK, Santosh MS. Physica B, 2010; 405:2078-2082

- [40] Cullity BD, Graham CD. Introduction to Magnetic Materials, IEEE Press – Wiley, Piscataway, NJ USA, 2nd edn., 2009, ch.11:383-389.
- [41] Abe K, Miyamoto Y, Chikazumi S, J. Phys. Soc. Japan, 1976; 41:1894-1902
- [42] Tiberto P, Barrera G, Celegato F, Coisson M, Chiolerio A, Martino P, Pandolfi P, Allia P. Eur. J. Phys. B, 2013; 86:173:1-173:6; DOI: 10.1140/epjb/e2013-30983-8
- [43] Knobel M, Nunes WC, L. Socolovsky M, De Biasi E, Vargas JM, Denardin JC. J. Nanosc. Nanotech., 2008; 8:2836-2857; DOI:10.1166/jnn.2008.017
- [44] Mamiya H, Ohnuma M, Nakatani I, Furubayashi T. IEEE Trans. Magnetics, 2005; 41:3394-3396; DOI: 10.1109/TMAG.2005.855205
- [45] Kachkachi H, Mahboub H. J. Magn. Magn. Mater., 2004; 278:334-341; DOI: 10.1016/j.jmmm.2003.12.1354
- [46] Allia P. J. Physics: Conf. Series, 2014; 521:012008:1-012008:4; DOI: 10.1088/1742-6596/521/1/012008
- [47] Allia P, Tiberto P. J. Nanopart. Res., 2011; 13:7277-7293; DOI: 10.1007/s11051-011-0642-2
- [48] Coral DF, Mendoza Zélis P, de Sousa ME, Muraca D, Lassalle V, Nicolás P, Ferreira ML, Fernández van Raap M B. J. Appl. Phys., 2014; 115:043907; DOI:10.1063/1.4862647
- [49] Abdallah HMI, Moyo T. J. Magn. Magn. Mater., 2014; 361:170-174; DOI: 10.1016/j.jmmm.2014.02.077